This is a preprint, the final version is subject to change, of the American Mineralogist (MSA)
Cite as Authors (Year) Title. American Mineralogist, in press.
DOI: https://doi.org/10.2138/am-2020-7271

# AM 7271 Revision 1

# Some geometrical properties of fission-track-surface intersections in apatite

RAYMOND JONCKHEERE[1,*], CAROLIN ASLANIAN[1], BASTIAN WAUSCHKUHN[1], AND LOTHAR RATSCHBACHER[1]

[1]Geologie, TU Bergakademie Freiberg, Bernhard-von-Cottastraße 2, 09599 Freiberg, Germany

## ABSTRACT

Parallel fission-track-surface intersections identify the grains in an etched apatite mount that have been polished parallel to their prism faces, and mark the orientations of their ***c***-axes. Their lengths in prism faces (*Dpar*) are a practical kinetic parameter that is indicative of the track annealing rate of the apatite. Little is known however about their geometrical properties in non-prism faces. We present a model calculation of the frequency distributions of the orientations, lengths, and widths of track-surface intersections in non-prism faces. The current model does not include the effects of surface etching or measurement imprecision. However, as far as it goes, it is consistent with measurements in apatite surfaces up to 30° to the ***c***-axis. Regardless of the model, we submit that the statistical properties of the fission-track-surface intersections have practical uses. The distribution of their orientations is characteristic of the orientation of the etched surface relative to the ***c***-axis. The distribution of their lengths presents a possible tool for investigating track etching, in particular for evaluating the fractions of tracks added and lost through surface etching. The distribution of their widths is a potential kinetic parameter independent of surface orientation and less susceptible to the factors, such as the sampling method and surface etch rate, that produce conflicting *Dpar*-values.

**Keywords**: Apatite, fission track, etching, Dpar, Dper, statistics.

*Email: Raymond.Jonckheere@geo.tu-freiberg.de, Orcid 0000-0003-0710-6265



Always consult and cite the final, published document. See http:/www.minsocam.org or GeoscienceWorld

# INTRODUCTION

Fission-track dating is based on counting the damage trails (fission tracks) produced by nuclear fission of uranium isotopes. Fission tracks in apatite have a length of ~20 μm (Jonckheere, 2003) and a maximum diameter of ~10 nm (Paul and Fitzgerald, 1992; Li et al., 2011; 2012; 2014). The mineral grains are mounted, polished, and etched. Etching widens the tracks to ~1 μm for observation and counting with an optical microscope. So, we do not count the tracks as such but the etched channels that develop along the track axes from their surface intersections. The model of fission track etching changed little in five decades (Price and Walker, 1962; Price and Fleischer, 1971; Tagami and O'Sullivan, 2005; Hurford, 2019). It describes track development as the result of two etch rates. The track etch rate $v_T$ along the track axis is the rate at which the damaged material in the track core is removed; the bulk etch rate $v_B$ is the rate at which the surrounding undamaged material is etched in all other directions. This etch model implies that the etching efficiency $\eta_E$ is a function of $v_B$ and $v_T$; in its simplest form:

$$\eta_E = 1 - \left(\frac{v_B}{v_T}\right)^2 \qquad (1)$$

For minerals, with anisotropic $v_B$, equation (1) is considered to hold for the value of $v_B$ perpendicular to the etched surface (surface etch rate $v_S$). Often, $\eta_E$ is taken to also be the fraction of tracks counted (counting efficiency $\eta_C$; Hasebe et al., 2004; Tagami and O'Sullivan, 2005). Although other studies are less explicit about the relationship between the counting and etching efficiencies, equation (1) is the basis for the common practice of counting the fission tracks in low-$v_B$ (high $\eta_E$) surfaces, such as the prism faces of apatite and zircon, characterized by sharp polishing scratches (Gleadow, 1978; 1981). The cleavage planes of muscovite are also considered to have near unit counting efficiencies. In contrast, there is theoretical and experimental evidence that the track counting efficiencies of these



Always consult and cite the final, published document. See http:/www.minsocam.org or GeoscienceWorld

surfaces are much lower (Jonckheere and Van den haute, 1998; 1999; 2002; Jonckheere, 2003; Enkelmann et al., 2005). This is thought to be due to an observation threshold, which prevents the observation or the confident identification of the shallowest etched tracks with an optical microscope. It is thus less than certain that apatite prism surfaces are ideal and other surfaces unsuited for counting tracks. In addition, the focus on prism faces limits the number of grains suitable for fission-track dating. This is most disadvantageous for sediment samples containing grains which seldom present their prism faces to the observer. This is the more serious because distinguishing the age components in a sediment sample for provenance studies requires dating a large number of grains ($\geqslant$117; Vermeesch, 2004).

It is therefore useful to investigate the properties of non-prism faces. Here, we examine how we can determine the orientations of non-prism faces relative to the mineral's ***c***-axis. The outline of a grain section and the orientation of inclusions provide useful indications, but are not always available or reliable. The grains are often rounded in transport, broken during mineral separation, free of inclusions, or contain inclusions with no preferential orientations. The etched-track-surface intersections provide a more dependable criterion. The track openings in a prism face are a constant length and oriented parallel to each other and to the ***c***-axis. Little is known about the track-surface intersections in other faces, other than that they are unlike those in prism faces. Like the shapes of the track channels, those of the track openings are determined by the etch rates of the crystal planes (radial shift rates $v_R$; Jonckheere et al., 2019). This implies that certain regularities of shape and size of the track openings must exist in all apatite faces. In the following, we attempt to relate the distributions of the orientations, lengths and widths of the track openings in apatite to the angle of the etched surface relative to the ***c***-axis. We propose a geometrical model, describe experiments carried out to test the model, and discuss the accord between model and data, before considering some practical applications.



Always consult and cite the final, published document. See http:/www.minsocam.org or GeoscienceWorld

## MODEL ASSUMPTIONS

We characterize a fission track intersecting a prism face by three parameters ($z$, $\phi$, $\theta$); $z$ is the depth of its lower endpoint below the surface, $\phi$ its angle to the ***c***-axis, and $\theta$ the angle between the surface and its projection on a basal plane (Figure 1a). The shape of the track opening is an elongated hexagon with length $b$ parallel and width $c$ perpendicular to *the **c**-axis*; $b$ thus corresponds to the kinetic parameter *Dpar* and $c$ to *Dper* (Donelick et al., 1999, 2005; Ketcham, 2003). The principal variables used in the following calculations are summarized in Table 1. Images show that $b$ (*Dpar*) is to a first approximation independent of either $\phi$ or $\theta$, and that $c$ (*Dper*) is independent of $\phi$, but increases with decreasing $\theta$ (Figure 1b). These two core assumptions are based on observations, but not unconnected to earlier results. The assumption that *Dpar* is independent of track orientation ($\phi$, $\theta$), or for that matter of the specific prism face in which the tracks are etched, is implicit in its use as a kinetic parameter dependent on the apatite composition but not on other factors (Donelick et al., 1999; 2005). It is also consistent with a recent etch model, in particular with the fact that prism faces contain periodic bond chains parallel to the ***c***-axis, but not in other orientations (Jonckheere et al., 2019). The contrasting assumption that *Dper* depends on $\theta$ (although not on $\phi$) is also consistent with this etch model. This follows from the fact that the intrinsic width $a$ of an etched track channel is controlled by the radial etch rate $v_R$ of the pair of prism planes flanking the track axis. The etch model thus implies that the true (minimum) channel width, $a$, is constant and its apparent width at the surface, *Dper*, is therefore a function of the angle $\theta$. As for *Dpar*, the second assumption implies that all apatite prism faces have the same etch rate although they are known not to be identical in all respects (Honess, 1927). It is nevertheless reasonable to assume for now that there exists little variation in their radial etch rates $v_R$, because the observed channel widths of tracks etched in an apatite basal surface shows no obvious dependence on the azimuth orientations of the tracks. Regardless of this theoretical support, it is more important that our core assumptions are verifiable by observation (Figure 1b).



Always consult and cite the final, published document. See http:/www.minsocam.org or GeoscienceWorld

## THE $\theta$-DISTRIBUTION

We consider tracks intersecting an internal apatite prism face. If $N$ is the number of tracks per unit volume then, for a homogeneous and isotropic track distribution, the number of tracks per unit surface area that have their lower endpoints in the interval $dz$ at depth $z$ is $N\,dz$. We collect them in a point on the Z-axis, perpendicular to the surface (Figure 2a and b). Assuming a constant track length $l$, the upper track endpoints are then distributed over a hemisphere with radius $l$ (porcupine geometry; Dakowski, 1978). The fraction of the ($N\,dz$) tracks in the angular interval ($d\theta$, $d\phi$) is proportional to the area $dS = (l\,d\theta)\,(l \sin\phi\,d\phi)$ (Figure 2c), so that the number of tracks in the interval ($dz$, $d\theta$, $d\phi$) is:

$$N_T(z,\theta,\phi)\,dz\,d\theta\,d\phi = N\,l^2 dz\,d\theta \sin\phi\,d\phi \qquad (2)$$

The tracks for which $\phi_1 \leqslant \phi \leqslant \pi - \phi_1$ intersect the surface (Figure 2a). Integrating (2) between these limits gives:

$$N_T(z,\theta)\,dz\,d\theta = 2\,N\,l^2\,d\theta \cos\phi_1\,dz \qquad (3)$$

From $t = l \sin\phi_1$ (Figure 2a) and $z = t \sin\theta$ (Figure 2b), it follows that $\sin\phi_1 = z / (l \sin\theta)$, and therefore:

$$N_T(z,\theta)\,dz\,d\theta = 2\,N\,l^2 d\theta\,[1 - (z/l \sin\theta)^2]^{1/2}\,dz \qquad (4)$$

Integrating (4) over $z$ for $z_1 = 0 \leqslant z \leqslant z_2 = l \sin\theta$ (substituting $x = z / l \sin\theta$, so that $dz = l \sin\theta\,dx$, $x_1(z_1) = 0$, and $x_2(z_2) = 1$) gives:

$$N_T(\theta)\,d\theta = \frac{\pi}{2}\,N\,l^3 \sin\theta\,d\theta \qquad (5)$$

Normalizing to the number of tracks intersecting a unit surface (½ $N\,l$), and setting a scaling factor $A = \pi\,l^2$, gives:



Always consult and cite the final, published document. See http:/www.minsocam.org or GeoscienceWorld

$$N_T(\theta)\, d\theta = A \sin\theta\, d\theta \qquad (6)$$

This defines the frequency distribution of the only parameter ($\theta$) that affects the track openings in a prism face.

Etching exhumes tracks below the polished surface, that begin to etch later than surface tracks and have smaller track openings. Exhumed tracks have a different $\theta$-distribution, $N_E(\theta)\, d\theta$, which is calculated as above. Ignoring the small fraction of tracks completely contained in the eliminated layer $d$ we obtain (Figure 2d):

$$N_E(\theta)\, d\theta = \pi\, d\, N\, l^2\, d\theta = B\, d\theta \qquad (7)$$

## GEOMETRICAL RELATIONSHIPS

The proposed model implies certain geometrical relationships between the shape and dimensions ($b$ = *Dpar*; $c$ = *Dper*) of the track-surface intersections in a prism face and the corresponding dimensions ($g$, $h$) and orientation ($\beta$) of the track-surface intersections in a face at an angle $\alpha$ to the ***c***-axis (Figure 3a, b). We observe that:

$$\tan\alpha = e/b \qquad \text{(8; Figure 3c)}$$

$$\cos\alpha = b/d \qquad \text{(9; Figure 3c)}$$

$$\tan\theta = e/f \qquad \text{(10; Figure 3d)}$$

$$\sin\theta = a/c \qquad \text{(11; Figure 3d)}$$

$$\tan\beta = f/d \qquad \text{(12; Figure 3e)}$$

$$\cos\beta = d/g \qquad \text{(13; Figure 3e)}$$

$$\cos\beta = h/c \qquad \text{(14; Figure 3e)}$$



Always consult and cite the final, published document. See http:/www.minsocam.org or GeoscienceWorld

From which it follows that:

$$\beta = \arctan\left(\frac{\sin\alpha}{\tan\theta}\right) \tag{15}$$

$$g/b = \sqrt{\frac{sin^2\,\theta + sin^2\,\alpha\; cos^2\,\theta}{cos^2\,\alpha\;\; sin^2\,\theta}} \tag{16}$$

$$\mathrm{h/a} = \sqrt{\frac{1}{\sin^2\theta + \sin^2\alpha\,\cos^2\theta}} \tag{17}$$

Figure 4 plots $\beta = \mathrm{f}(\theta)$ (4a), $(g/b) = \mathrm{f}(\theta)$ (4b), and $(h/a) = \mathrm{f}(\theta)$ (4c) for $\alpha = 1$, 5, 10, 20, and 30°. Equation (15) predicts that $\beta$ increases with increasing $\alpha$ and decreasing $\theta$. This implies that also the range of orientations of the surface intersections of a track population broadens as the surface is inclined at a larger angle $\alpha$ to the ***c***-axis. Figure 5 illustrates this in a qualitative manner. Figure 5 also confirms that the range of lengths $g$ increases with increasing $\alpha$, whereas the widths $h$ are little affected by $\alpha$, although this is less obvious from equations (16) and (17). Figure 6 illustrates the effect of the dip angle $\theta$. It depicts the same tracks in an apatite surface at 10° to the ***c***-axis in reflected (6a) and transmitted (6b) light. The ***c***-axis runs from left to right and the intersections of tracks dipping to the east or west are aligned with it. However, those of tracks dipping to the south are rotated clockwise, whereas those of tracks dipping to the north are rotated anti-clockwise, consistent with Figure 4a. One can also see that the rotation angle $\beta$ is greater for shallower dipping tracks ($\theta$; equation 15).

## FREQUENCY DISTRIBUTIONS

We use (15)-(17) to derive the distributions of $\beta$, $(g/b)$, and $(h/a)$ from the $\theta$-distribution (equation (6)). We have that:



Always consult and cite the final, published document. See http:/www.minsocam.org or GeoscienceWorld

$$N_T(\beta)\, d\beta = N_T(\theta) d\theta \left|\frac{d\theta}{d\beta}\right| d\beta \tag{18}$$

This gives (Appendix A1):

$$N_T(\beta)\, d\beta = \frac{A\ \sin^2\alpha\ \cos\beta}{[\sin^2\beta + \sin^2\alpha\ \cos^2\beta]^{3/2}}\ d\beta \tag{19}$$

Likewise, for $(g/b)$:

$$N_T(g/b)\, d(g/b) = N_T(\theta) d\theta \left|\frac{d\theta}{d(g/b)}\right| d(g/b) \tag{20}$$

Which gives (Appendix A2):

$$N_T(g/b)\, d(g/b) = \frac{A\,(g/b)\tan^2\alpha}{[((g/b)^2-1) - \tan^2\alpha]^{1/2}\,[(g/b)^2-1]^{3/2}}\ d(g/b) \tag{21}$$

And finally for $(h/a)$:

$$N_T(h/a)\, d(h/a) = N_T(\theta) d\theta \left|\frac{d\theta}{d(h/a)}\right| d(h/a) \tag{22}$$

Which gives (Appendix A3):

$$N_T(h/a)\, d(h/a) = \frac{A/\cos\alpha}{(h/a)^2\,[(h/a)^2-1]^{1/2}}\ d(h/a) \tag{23}$$

Figure 7 plots the distributions of the orientations of the major axes of the track openings relative to the ***c***-axis ($N_T(\beta)\, d\beta$; 7a), of the major axes lengths ($N_T(g/b)$ d$(g/b)$; 7b), and the minor axes lengths of the track openings ($N_T(h/a)$ d$(h/a)$; 7c) in apatite surfaces at $\alpha$ = 1, 5, 10, 20 and 30° to a prism face.

A similar calculation gives the distributions of $\beta$, $(g/b)$, and $(h/a)$ for tracks exhumed in the course of etching (Appendix A4):



Always consult and cite the final, published document. See http:/www.minsocam.org or GeoscienceWorld

$$N_E(\beta)\, d\beta = \frac{B\ \sin\alpha}{\sin^2\beta + \sin^2\alpha\ \cos^2\beta}\, d\beta \qquad (24)$$

$$N_E(g/b)\, d(g/b) = \frac{B\ (g/b)\ \tan\alpha}{[((g/b)^2 - 1) - \tan^2\alpha\,]^{1/2}\,[(g/b)^2 - 1\,]}\, d(g/b) \qquad (25)$$

$$N_E(a/h)\, d(a/h) = \frac{B\ /\ (h/a)\cos^2\alpha}{[(h/a)^2 - 1]^{1/2}\,[(1 - (h/a)^2\ \sin^2\alpha)]^{1/2}}\, d(a/h) \qquad (26)$$

Figure 8 plots the distributions, $N_E(\beta)\, d\beta$, of $\beta$, $N_E(g/b)$ d$(g/b)$, of $(g/b)$, and, $N_E(h/a)$ d$(h/a)$, of $(h/a)$ for $\alpha$ = 1, 5, 10, 20 and 30°.

## EXPERIMENTAL EVIDENCE

We cut sections at 0, 10, 20, and 30° to the ***c***-axis of an unannealed Durango apatite containing fossil tracks. Each section was mounted and polished with 6, 3, and 1 μm diamond suspensions. A final nano-polish with 0.04 μm silica suspension ensured that the surfaces showed no or a few faint polishing scratches, even after etching. Progress was checked after each step with a microscope with Nomarski differential interference contrast. After ultrasonic cleaning and drying in a curing cabinet at 35 °C, the samples were etched for 20 s in 5.5 M $HNO_3$ at 21 °C (Carlson et al., 1999) to reveal the tracks.

Figure 5 shows the track openings in sections at 0, 10, 20, and 30° to the ***c***-axis. Those in the prism surface are a fixed length and aligned parallel to ***c*** (Figure 5a). Those in the surface at 10° to ***c*** have somewhat variable lengths and a limited range of and orientations about the ***c***-axis azimuth (Figure 5b). The surfaces at 20° (Figure 5c) and 30° (Figure 5d) are characterized by an increasing range of sizes and orientations. There is still a clear preferential orientation but it becomes more difficult to infer the ***c***-axis orientation. The track openings in these surfaces can still be described as slit-like but this is not the case for all orientations. Those in pyramidal and basal faces, for instance, do not have



Always consult and cite the final, published document. See http:/www.minsocam.org or GeoscienceWorld

elongated shapes to which an unambiguous length, width and orientation can be assigned (Jonckheere and Van den haute, 1996). This implies that there is a limit to a model, which aims to establish geometrical relationships between the track openings in a prism surface and surfaces at given angles to it, in which the influence of the etching properties of other low-index prism planes and of the basal plane can be ignored (Jonckheere et al., 2019). It is thus an approximate two-dimensional solution to a three-dimensional problem, and an angle α of 30° is close to, even at the limit, of its applicable range.

The etched sections were inspected with a Zeiss AxioImager Z2m microscope at a magnification of 1250× (50× objective, 10× oculars, 2.5× post-magnification). Between 50 and 100 reflected-light images were taken of each section with a Zeiss ICc3 digital camera connected to a computer running Autoscan TrackWorks. The images were analysed with the Fiji (ImageJ) software (National Institutes of Health and Laboratory for Optical and Computational Instrumentation; University of Wisconsin; USA). Each image was converted to 8-bit and thresholded to separate the dark track openings from the light background. The thresholded images were binarized and features with an area of >25 pixels extracted, in order to avoid point-like objects being identified as tracks. A total of 8416 items were identified in the four samples. This dataset contains a small fraction of artefacts, due to track overlap, very short and wide tracks being assigned an incorrect orientation, and, rarely, due to a small foreign object, e.g. a speck of dust. This hands-off approach eliminates the need for complicated processing and avoids the possible associated biases. Mismeasured features constitute a negligible fraction of the data, and can be identified in the data plots. The Fiji software offers detailed feature statistics, of which we used the maximum and minimum Feret diameters[1] for the lengths and widths of the track openings, and the orientation of the major axis of a fitted

[1] The maximum and minimum Feret are the longest and shortest straight lines between two points along the edge of a thresholded feature.



Always consult and cite the final, published document. See http:/www.minsocam.org or GeoscienceWorld

ellipse for that of the long axis of the track openings. The latter choice was necessitated by the fact that the orientation of the maximum Feret diameter is unreliable in certain directions (0° and 90° in the image), likely due to the manner in which it is calculated. Apart from that, the maximum and minimum Feret diameters correlate closely with the lengths of the major and minor ellipse axes. There is no self-evident method for obtaining reliable numerical estimates of the accuracy and precision of our measurements. The lengths and widths of track-surface intersections observed in high-magnification microscope images are difficult to define other than as their measured values. Our work is also less concerned with their absolute dimensions than their variation with angle to the ***c***-axis (eq. 21 and 23). The images contain too few tracks for reproducibility estimates (Figure 5). The results show that the fraction of misoriented features is next to negligible and the error is in general $\ll 5°$.

## RESULTS AND DISCUSSION

Figure 9 plots the frequencies of the measured orientations ($\beta$-distribution), lengths ($g$-distribution) and widths ($h$-distribution) of the track openings. A numerical comparison with the theoretical distributions is not possible because the equations do not include the effects of measurement error or loss or gain of tracks due to surface etching, both of which are unknown at this stage. For scaling the model to the length and width data, we assumed that *Dpar* = 1.81 μm and *Dpe*r = 0.63 μm. These are by far the values with the highest frequencies in the dataset for the prism section ($\alpha$ = 0°). The *Dpar*-value agrees with that reported for Durango apatite in several studies using the same etching conditions (1.91(14) μm: Carlson et al., 1999; 1.83(13) μm: Donelick et al., 1999; all *Dpar*: 1.82(3) μm, typical *Dpar*: 2.05(2) μm: Sobel and Seward, 2010; 1.5-2.1 μm: Ketcham et al., 2015); our *Dper* estimate, in contrast, is somewhat high compared to that (0.43(13) μm) reported for Durango apatite by Donelick et al. (1999).



Always consult and cite the final, published document. See http:/www.minsocam.org or GeoscienceWorld

In broad terms, and within its known limitations, our model appears to be in general agreement with the data. The $\beta$-distribution is narrow for the prism face (all track openings parallel to the ***c***-axis) and broadens more or less as predicted with increasing angle $\alpha$ to ***c*** (Figure 7a). The $\beta$-distribution for $\alpha = 30°$ appears tighter than expected. This could be an indication that the model reaches a limit, due to the interference from adjoining low-index prism faces. The $g$-distribution is in agreement with the model insofar as that it is narrow for the prism face and its right flank broadens and shifts to higher $g$-values with increasing angle to the ***c***-axis (Figure 7b). The $g$-distributions are however broader than predicted and left-skewed. The broadening is understood as a result of data scatter, due to variations in the conditions for capturing the images and thresholding. The skewness is in part due to the addition of tracks as a result of surface etching at a rate $v_S$. This is consistent with the fact that the left tail of the $g$-distribution grows with increasing angle $\alpha$ to the ***c***-axis because $v_S$ increases with increasing $\alpha$ (Jonckheere et al., 2019). The left tails of the $g$-distributions are on the other hand not flat, as one would expect for surface etching at constant $v_S$. The increasing $g$-frequencies up to 1.81 μm could be due to the fact that $v_S$ decreases during etching due to decreasing polishing damage with increasing depth below the initial surface. The rate of track addition and loss during etching is important for fission-track dating, and experiments combining measurements of the track openings with step etching would be useful. It should however not be assumed that exhumation of tracks is the sole possible cause of undersized track openings. Figure 1b (track 4) shows an undersized etch pit in a prism face; the absence of a long track channel distinguishes it from an exhumed track. This particular etch pit appears to be the remnant of a shallow track gradually being eliminated by surface etching (Jonckheere and Van den haute, 1996; Stübner et al., 2008). It is also not excluded that short (low-$v_T$) terminal track sections (Jonckheere et al., 2017; Tamer et al., 2019) could produce shallow undersized etch pits where they intersect the surface, but this is at present conjecture.



Always consult and cite the final, published document. See http:/www.minsocam.org or GeoscienceWorld

The $h$-distributions are consistent with our model insofar as that they are right-skewed with a maximum around 0.63 μm and almost independent of the orientation $\alpha$ of the etched surface (Figure 7c). The $h$-values below the maximum at 0.63 μm are again thought to result from data noise and surface etching.

Figure 10 plots the $\beta$- ($\beta$-spectrum), $g$- ($g$-spectrum), and $h$-values ($h$-spectrum) against their rank. Although the spectra show the same data as the distributions in Figure 9, they present a practical means of characterizing an apatite surface, independent of a geometrical etch model. The $\beta$-spectra are S-shaped for all surface orientations. The midsection for the prism face is flat, indicating that the track openings are parallel. Deviations to either side are due to small or overlapping track openings, whose orientations were not determined accurately, and to a few non-track features. The $\beta$-spectra become steeper with increasing angle to the $\boldsymbol{c}$-axis. Thus a $\beta$-spectrum permits to infer the azimuth and the dip of the $\boldsymbol{c}$-axis. The central estimate defines its azimuth and the dispersion reflects its dip. It is at this stage uncertain if the $\boldsymbol{c}$-axis orientations can be determined with enough accuracy and precision for practical studies, or how many measurements are needed to establish a $\beta$-spectrum. On the other hand, track openings can be measured automatically with current fission-track software, perhaps requiring a minor extension to collect the relevant statistics (Gleadow, 2009; Gleadow et al., 2019).

The $g$-spectra are also S-shaped but difficult to interpret. Their midsections (second and third quartiles) are quite straight and steeper at greater angles to the $\boldsymbol{c}$-axis. Our model predicts that $g$ increases with $\alpha$ but never decreases below *Dpar* (Figure 7b). However, the $g$-spectra contain a large fraction of tracks shorter than the reference value (*Dpar* = 1.81 μm). Considering that the data are cut off at $g \approx 0.5$ μm, close to a fifth of the tracks in the prism face are below the reference. The fractions of both the oversized and undersized tracks increase with angle to the $\boldsymbol{c}$-axis. Increases in the size of the track openings are accounted for by our model, at least in qualitative terms. At this



Always consult and cite the final, published document. See http:/www.minsocam.org or GeoscienceWorld

stage, most of the undersized tracks must be attributed to the gradual exhumation of tracks due to surface etching, which is not included in our model. The increasing fraction of undersized track openings is consistent with the assumption of a higher surface etch rate $v_S$ at larger angles to the ***c***-axis (Jonckheere et al., 2019). The large excess of undersized track openings suggests that it is possible that unidentified factors must be considered to explain it in quantitative detail. Our current results nevertheless suggest that the *g*-spectra provide useful tools for investigating the etching characteristics of different apatite surfaces, with a potential for determining surface etch rates and the rates of addition and loss of tracks. The *g*-spectrum of the prism face suggests that the different *Dpar*-values reported in an inter-laboratory experiment (Ketcham et al., 2015) may be related to the sampling method (random *vs*. representative; Sobel and Seward, 2010), but also to surface etching dependent on the polishing procedures.

The *h*-spectra are also S-shaped, and, considering the scale, quite flat. They are little affected by surface etching or by the orientation α of the etched surface relative to the apatite ***c***-axis. Therefore, *h*-spectra could prove to be a useful kinetic parameters (Donelick et al., 1999; Ketcham et al., 1999), in particular when considering track counts or length measurements in apatite surfaces other than the prism faces.

## IMPLICATIONS

Our measurements provide experimental data related to the lengths, widths, and orientations of the fission-track-surface intersections in different apatite surfaces. The results are in reasonable agreement with the proposed model. We submit that this model provides a basis for understanding fission-track etching in apatite although it needs to be extended to include the effects of surface etching in a quantitative manner, as well as the effects of measurement uncertainties. A further aim is to formulate a full 3D model.



Always consult and cite the final, published document. See http:/www.minsocam.org or GeoscienceWorld

We propose that measurements of fission-track-surface intersections have possible practical uses. The distribution of their orientations is characteristic of orientation of the etched surface relative to the ***c***-axis. The distribution of their lengths constitutes a new tool for investigating track etching in apatite, in particular for evaluating the fractions of tracks added and lost by surface etching. The distribution of their widths is a possible kinetic parameter independent of surface orientation, and less sensitive to the factors, such as sampling method and surface etch rate, that produce inconsistent *Dpar*-values.

A further perspective is based on evidence that internal apatite prism faces do not have unit track counting efficiencies (Jonckheere and Van den haute, 2002; Jonckheere, 2003; Jonckheere et al., 2015). The present results suggest that prism surfaces also do not have negligible, or constant, etch rates. It is therefore interesting to consider if other surface orientations can be used for fission-track dating and confined-track length measurements. Their usefulness would depend on whether their orientations to the ***c***-axis and track counting efficiencies can be determined with fission-track equipment. We anticipate that a more detailed investigation of the track-surface intersections can provide these estimates. Even at the cost of some loss of precision, this might still be a valuable development for dating sediment samples, in which the grains are seldom polished parallel to their prism faces, and a large number must be dated for distinguishing age components (Vermeesch, 2004; 2019; Galbraith, 2005).

## ACKNOWLEDGMENT AND FUNDING

Research funded by the German Research Council (DFG project Jo 358/4-1). This contribution owes much to the careful and insightful reviews of R. Ketcham and R. Arató. We are grateful to our palaeontologist colleagues for the occasional peace and quiet which allowed us to complete this investigation.



Always consult and cite the final, published document. See http:/www.minsocam.org or GeoscienceWorld

## REFERENCES CITED

Carlson, W.D., Donelick, R.A., and Ketcham, R.A., 1999. Variability of apatite fission-track annealing kinetics: I. Experimental results. American Mineralogist 84, 1213-1223.

Dakowski, M., 1978. Length distributions of fission tracks in thick crystals. Nuclear Track Detection 2, 181-189.

Donelick, R.A., Ketcham, R.A., and Carlson, W.D., 1999. Variability of apatite fission-track annealing kinetics: II. Crystallographic orientation effects. American Mineralogist 84, 1224-1234.

Donelick, R.A., O'Sullivan, P.B., and Ketcham, R.A., 2005. Apatite fission-track analysis. Reviews in Mineralogy and Geochemistry 58, 49-94.

Enkelmann, E., Jonckheere, R., and Wauschkuhn, B., 2005. Independent fission-track ages (ϕ-ages) of proposed and accepted apatite age standards and a comparison of ϕ-, Z-, ζ- and $\zeta_0$-ages: implications for method calibration. Chemical Geology 222, 232-248.

Galbraith, R., 2005. Statistics for fission track analysis. Chapman and Hall/CRC, Taylor and Francis Group, Boca Raton, Florida, USA, pp. 219.

Gleadow, A.J.W., 1978. Anisotropic and variable track etching characteristics in natural sphenes. Nuclear Track Detection 2, 105-111.

Gleadow, A.J.W., 1981. Fission track dating methods: what are the real alternatives? Nuclear Tracks 5, 3-14.

Gleadow, A.J.W., 2009. Coincidence mapping - A key strategy for the automatic counting of fission tracks in natural minerals. Geological Society, London, Special Publications, 324, 25-36.



Always consult and cite the final, published document. See http:/www.minsocam.org or GeoscienceWorld

Gleadow, A., Harrison, M., Kohn, B., Lugo-Zazueta, R., and Phillips, D., 2015. The Fish Canyon Tuff: A new look at an old low-temperature thermochronology standard. Earth and Planetary Science Letters 424, 95–108.

Gleadow, A., Kohn, B., and Seiler, C., 2019. The future of fission-track thermochronology. In: Malusà M.G. and Fitzgerald P.G. (eds.), Fission-Track Thermochronology and its Application to Geology, Springer Textbooks in Earth Sciences, Geography and Environment, 77-92.

Hasebe, N., Barbarand, J., Jarvis, K., Carter, A., and Hurford, A.J., 2004. Apatite fission-track chronometry using laser ablation ICP-MS. Chemical Geology 207, 135–145.

Hurford, A.J., 2019. An historical perspective on fission-track thermochronology. In: Malusà M.G. and Fitzgerald P.G. (eds.), Fission-Track Thermochronology and its Application to Geology, Springer Textbooks in Earth Sciences, Geography and Environment, 3-23.

Jonckheere, R., 2003. On the densities of etchable fission tracks in a mineral and co-irradiated external detector with reference to fission-track dating of minerals. Chemical Geology 200, 41-58.

Jonckheere, R., and Van den haute, P., 1996. Observations on the geometry of etched fission tracks in apatite: implications for models of track revelation. American Mineralogist 81, 1476-1493.

Jonckheere, R., and Van den haute, P., 1998. On the frequency distributions per unit area of the dimensions of fission tracks revealed in an internal and external mineral surface and in the surface of an external detector. Radiation Measurements 29, 135-143.

Jonckheere, R., and Van den haute, P., 1999. On the frequency distributions per unit area of the projected and etchable lengths of surface-intersecting fission tracks: Influences of track revelation, observation and measurement. Radiation Measurements 30, 155-179.



Always consult and cite the final, published document. See http:/www.minsocam.org or GeoscienceWorld

Jonckheere, R., and Van den haute, P., 2002. On the efficiency of fission-track counts in an internal and external apatite surface and in a muscovite external detector. Radiation Measurements 35, 29-40.

Jonckheere, R., Van den haute, P., and Ratschbacher, L., 2015. Standardless fission-track dating of the Durango apatite age standard. Chemical Geology 417, 44-57.

Jonckheere, R., Wauschkuhn, B., and Ratschbacher, L., 2019. On growth and form of etched fission tracks in apatite: A kinetic approach. American Mineralogist 104, 569-579.

Ketcham, R.A., 2003. Observations on the relationship between crystallographic orientation and biasing in apatite fission-track measurements. American Mineralogist 88, 817-829.

Ketcham, R.A., Carter, A., and Hurford, A.J., 2015. Inter-laboratory comparison of fission track confined length and etch figure measurements in apatite. American Mineralogist 100, 1452-1468.

Ketcham, R.A., Donelick, R.A., and Carlson, W.D., 1999. Variability of apatite fission-track annealing kinetics III: extrapolation to geological time scales. American Mineralogist 84, 1235-1255.

Li, Weixing, Kluth, P., Schauries, D., Rodriguez, M.D., Lang, M., Zhang, Fuxiang, Zdorovets, M., Trautmann, C., and Ewing, R.C., 2014. Effect of orientation on ion track formation in apatite and zircon. American Mineralogist 99, 1127–1132.

Li, Weixing, Lang, M., Gleadow, A.J.W., Zdorovets, M.V., Ewing, R.C., 2012. Thermal annealing of unetched fission tracks in apatite. Earth and Planetary Science Letters 321-322, 121–127.

Li, Weixing, Wang, Lumin, Lang, M., Trautmann, C., Ewing, R.C., 2011. Thermal annealing mechanisms of latent fission tracks: Apatite *vs*. zircon. Earth and Planetary Science Letters 302, 227-235.



Always consult and cite the final, published document. See http:/www.minsocam.org or GeoscienceWorld

Paul, T.A., and Fitzgerald, P.G., 1992. Transmission electron microscopic investigation of fission tracks in fluorapatite. American Mineralogist 77, 336-344.

Price, P.B., and Fleischer, R.M., 1971. Identification of energetic heavy nuclei with solid dielectric track detectors: Applications to astrophysical and planetary studies. Annual Review of Nuclear Science 21, 95-334.

Price, P.B., and Walker, R.M., 1962. Chemical etching of charged-particle tracks in solids. Journal of Applied Physics 33, 3407-3412.

Sobel, E.R., and Seward, D., 2010. Influence of etching conditions on apatite fission-track etch pit diameter. Chemical Geology 271, 59-69.

Stübner, K., Jonckheere, R., and Ratschbacher, L., 2008. Revelation of nuclear tracks and dislocations: A Monte Carlo simulation of mineral etching. Geochimica et Cosmochimica Acta 72, 3184-3199.

Tagami, T., and O'Sullivan, P.B., 2005. Fundamentals of fission-track thermochronology. Reviews in Mineralogy and Geochemistry 58, 19-47.

Tamer, M.T., Chung, L., Ketcham, R.A., Gleadow, A.J.W., 2019. Analyst and etching protocol effects on the reproducibility of apatite confined fission-track length measurement, and ambient-temperature annealing at decadal timescales. American Mineralogist, 104, 1421-1435.

Vermeesch, P., 2004. How many grains are needed for a provenance study? Earth and Planetary Science Letters 224, 441-451.

Vermeesch, P., 2019. Statistics for fission-track thermochronology. In: Malusà M.G. and Fitzgerald P.G. (eds.), Fission-Track Thermochronology and its Application to Geology, Springer Textbooks in Earth Sciences, Geography and Environment, 109-122.



Always consult and cite the final, published document. See http:/www.minsocam.org or GeoscienceWorld

**Table 1.** Most important variables

| Variable | Meaning | Figure |
|---|---|---|
| $l$ | Etchable track length. | 2a-2d |
| $z$ | Depth of the lower endpoint of an etched surface track below the apatite surface. | 1a; 2b |
| $\phi$ | Angle between the track axis and the apatite ***c***-axis. | 1a; 2c |
| $\theta$ | Angle between the projection of a track on a basal plane and the apatite surface. | 2b; 2d |
| $a$ | Width of the track channel, i.e., the minimum distance between the flanking prism planes. | 3c |
| $b$ | Long axis (maximum Feret) of a track intersection with an etched prism surface (*Dpar*). | 3c |
| $c$ | Short axis (minimum Feret) of a track intersection with an etched prism surface (*Dper*). | 3d |
| $d, e, f$ | Projected dimensions of the track openings permitting to relate ($g$, $h$) to ($b$, $a$). | 3c-3e |
| $\alpha$ | Angle between an etched apatite surface and the ***c***-axis. | 3b; 3c |
| $\beta$ | Angle between the long axis of a track opening and the orthogonal projection of the ***c***-axis on the etched surface ($\beta = 0$ for $\alpha = 0$). | 3b; 3e |
| $g$ | Long axis (maximum Feret) of the intersection of a track with an etched surface at an angle $\alpha$ to the ***c***-axis ($g = Dpar$ for $\alpha = 0$). | 3e |
| $h$ | The short axis (minimum Feret) of the intersection of a track with an etched surface at an angle $\alpha$ to the ***c***-axis ($h = Dper$ for $\alpha = 0$). | 3e |
| $N_T(\theta)\, d$<br>$N_E(\theta)\, d\theta$ | Frequency distributions of the angle $\theta$ of surface tracks (subscript T) and exhumed tracks (subscript E). | - |
| $N_T(\beta)\, d\beta$<br>$N_E(\beta)\, d\beta$ | Frequency distributions of the orientations of the openings of surface tracks (subscript T) and exhumed tracks (subscript E) in prism and non-prism faces. | 7a; 8a |
| $N_T(g/b)\, d(g/b)$<br>$N_E(g/b)\, d(g/b)$ | Frequency distributions of the lengths of the openings of surface tracks (T) and exhumed tracks (E) in prism and non-prism faces, normalized to those in a prism face ($b = Dpar$). | 7b; 8b |
| $N_T(h/a)\, d(h/a)$<br>$N_E(h/a)\, d(h/a)$ | Frequency distributions of the widths of the openings of surface tracks (T) and exhumed tracks (E) in prism and non-prism faces, normalized to that of the track channel ($a$). | 7c; 8c |



Always consult and cite the final, published document. See http:/www.minsocam.org or GeoscienceWorld

# FIGURE CAPTIONS

**Figure 1.** (**a**) A track intersecting a prism face is characterized by the depth $z$ of its lower endpoint below the surface, its angle $\phi$ to the ***c***-axis, and the angle $\theta$ between the prism surface and its projection on a basal plane. (**b**) Basis of the model; reflected- and transmitted-light image of fission tracks intersecting a prism face of Durango apatite, showing the alignment of the track openings parallel to the ***c***-axis and the effects of their depth $z$ and orientation ($\phi$, $\theta$). Etching conditions: 20 s in 5.5 M $HNO_3$ at 21 °C; (1) the slight increase of *Dpar* of tracks with a very small $\phi$ is neglected at this stage; (2) increasing width of the track-surface intersection with decreasing $\theta$; (3) rare overlapping track-surface intersections giving rise to erroneous measurements; (4) shallow track with undersized *Dpar*.

**Figure 2.** Porcupine arrangement in which the endpoints of tracks terminating within the layer $dz$ at depth $z$ below the surface are shifted parallel to the surface to a point on the Z-axis, perpendicular to the surface. This affects none of their properties ($z$, $\phi$, $\theta$) other than their positions. Their upper end-points are then distributed over the surface of a hemisphere with radius equal to the track length $l$ (outer circle); the sector above the apatite surface is shaded grey. (**a**) View perpendicular to a prism face, highlighting the wedge d$\theta$ (AB; green) of surface-intersecting tracks. Their projection on a basal plane encloses an angle $\theta$ with the surface and their minimum angle to the ***c***-axis is $\phi_1$. (**b**) View along the ***c***-axis, showing the interval $dz$ (dashed) at depth $z$ containing the track terminations, and, highlighted in green, the tracks at an angle $\theta$ to the surface that also intersect it; $t$ allows to relate $\phi_1$ in (a) to $\theta$ in (b). (**c**) Calculation of the number of tracks in the angular interval ($d\theta$, $d\phi$). (**d**) Inverted porcupine for calculating the $\theta$-distribution of tracks exhumed during etching; view along the ***c***-axis, similar to (b); the endpoints of tracks terminating within the layer $d$ removed by etching are drawn



Always consult and cite the final, published document. See http:/www.minsocam.org or GeoscienceWorld

together at the Z-axis; their other endpoints are then distributed over the surface of an inverted hemisphere.

**Figure 3.** Relationship between the orientation ($\beta$), length ($g$), and width ($h$) of track intersections with a surface at an angle $\alpha$ to the ***c***-axis, and the orientation, length ($b$), and width ($a$) of the intersection of a perpendicular track (θ= 90°) with the prism face. (**a**) Schematic crystal showing the ***c***-axis, basal plane, prism plane and the plane at an angle $\alpha$ to the ***c***-axis. (**b**) Sample cut at an angle $\alpha$ to the ***c***-axis showing track openings parallel to and at an angle $\beta$ to the projection of the ***c***-axis onto the observation plane; the labelled symbols indicate the directions in which the tracks and their openings are viewed in panels (c), (d) and (e). (**c**) View of the tracks perpendicular to the ***c***-axis; (**d**) view along the ***c***-axis, indicating the angle $\theta$. (**e**) View perpendicular to the cut surface, which is at an angle $\alpha$ to the ***c***-axis. The right-angled triangles highlighted in green are the basis for deriving equations (8)-(14).

**Figure 4.** Calculated relationships between (**a**) the orientations $\beta$, (**b**) the lengths ($g/b$), and (**c**) the widths ($h/a$) of the track openings and the angle $\theta$ of tracks etched in surfaces at 1, 5, 10, 20, and 30° to the ***c***-axis.

**Figure 5.** Enhanced-contrast reflected-light microscope images of the track openings in etched apatite surfaces at 0°, 10°, 20°, and 30° to the ***c***-axis (etching conditions: 20s in 5.5.M $HNO_3$ at 21°C). The images illustrate the increasing ranges of their sizes and orientations with increasing angle to the ***c***-axis.

**Figure 6.** Enhanced-contrast reflected-light (**a**) and transmitted-light (**b**) microscope images of the same fission tracks in an etched apatite surface at 10° to the ***c***-axis (etching conditions: 20s in 5.5.M $HNO_3$ at 21°C). The images illustrate that the sense and degree of rotation of the track-surface



Always consult and cite the final, published document. See http:/www.minsocam.org or GeoscienceWorld

intersections is correlated with the direction and steepness of the dip of the corresponding track channels.

**Figure 7.** Calculated frequency distributions of (**a**) the orientations $\beta$, (**b**) the lengths ($g/b$), and (**c**) the widths ($h/a$) of the intersections of surface tracks with apatite surfaces at 1, 5, 10, 20, and 30° to the ***c***-axis.

**Figure 8.** Calculated frequency distributions of (**a**) the orientations $\beta$, (**b**) the lengths ($g/b$), and (**c**) the widths ($h/a$) of the intersections of exhumed tracks with apatite surfaces at angles of 1, 5, 10, 20, and 30° to the ***c***-axis.

**Figure 9.** Measured frequency distributions of the orientations ($\beta$), lengths ($g$), and widths ($h$) of the intersections of all etched fission tracks with apatite surfaces at angles of 1, 5, 10, 20, and 30° to the ***c***-axis.

**Figure 10.** Spectra of the orientations ($\beta$), lengths ($g$), and widths ($h$) of the intersections of all etched tracks with apatite surfaces at 0, 10, 20, and 30° to the ***c***-axis. The dashed lines are the model minima.



Always consult and cite the final, published document. See http:/www.minsocam.org or GeoscienceWorld

# APPENDICES

Appendix A1. The $\beta$-distribution, $N_T(\beta)\ d\beta$

We derive the $\beta$-distribution, $N_T(\beta)\ d\beta$, from the $\theta$-distribution, $N_T(\theta)\ d\theta$ (equation (6)) using the Jacobian $|d\theta/d\beta|$, as follows:

$$N_T(\beta)\ d\beta = N_T(\theta) d\theta\ \left|\frac{d\theta}{d\beta}\right|\ d\beta \tag{A1}$$

$$N_T(\beta)\ d\beta = A\ \sin\theta\ \left|\frac{d\theta}{d\beta}\right|\ d\beta \tag{A2}$$

It follows from equations (6)-(8) and (10) that:

$$\tan\theta = \sin\alpha\ \cot\beta \tag{A3}$$

Or:

$$\theta = \arctan(\sin\alpha\ \cot\beta) \tag{A4}$$

Differentiating (A4) with respect to $\beta$ gives:

$$\left|\frac{d\theta}{d\beta}\right| = \frac{\sin\alpha}{\sin^2\beta + \sin^2\alpha\ \cos^2\beta} \tag{A5}$$

On the other hand, it follows from (A3) that:

$$\sin\theta = \sqrt{\frac{\sin^2\alpha\ \cos^2\beta}{\sin^2\beta + \sin^2\alpha\ \cos^2\beta}} \tag{A6}$$

Substituting (A5) and (A6) in (A2) gives:

$$N_T(\beta)\ d\beta = \frac{A\ \sin^2\alpha\ \cos\beta}{[\sin^2\beta + \sin^2\alpha\ \cos^2\beta]^{3/2}}\ d\beta \tag{A7}$$

Appendix A2. The $(g/b)$-distribution, $N_T(g/b)\ d(g/b)$



Always consult and cite the final, published document. See http:/www.minsocam.org or GeoscienceWorld

We derive the $(g/b)$-distribution, $N_T(g/b)\ d(g/b)$, from the $\theta$-distribution, $N_T(\theta)\ d\theta$ (equation (6)), as follows:

$$N_T(g/b)\ d(g/b) = A \sin\theta \left|\frac{d\theta}{d(g/b)}\right| d(g/b) \qquad \text{(A8)}$$

It follows from equation (16) that:

$$\sin\theta = \frac{\tan\alpha}{[(g/b)^2 - 1\,]^{1/2}} \qquad \text{(A9)}$$

and:

$$\theta = arcsin\left[\frac{\tan\alpha}{[(g/b)^2 - 1\,]^{1/2}}\right] \qquad \text{(A10)}$$

Differentiating (A10) with respect to $(g/b)$ gives:

$$\left|\frac{d\theta}{d(g/b)}\right| = \frac{(g/b)\ \tan\alpha}{[((g/b)^2 - 1) - \tan^2\alpha\,]^{1/2}\,[(g/b)^2 - 1\,]} \qquad \text{(A11)}$$

Substituting (A9) and (A11) in (A8) gives:

$$N_T(g/b)\ d(g/b) = \frac{A\,(g/b)\tan^2\alpha}{[((g/b)^2 - 1) - \tan^2\alpha]^{1/2}\,[(g/b)^2 - 1]^{3/2}}\ d(g/b) \qquad \text{(A12)}$$

<u>Appendix A3</u>. The $(h/a)$-distribution, $N_T(h/a)\ d(h/a)$

The equations are more manageable if we first derive the $(a/h)$-distribution, $N_T(a/h)$ d$(a/h)$, from the $\theta$-distribution $N_T(\theta)\ d\theta$:

$$N_T(a/h)\ d(a/h) = A \sin\theta \left|\frac{d\theta}{d(a/h)}\right| d(a/h) \qquad \text{(A13)}$$

It follows from equation (17) that:

$$\sin\theta = \frac{[(a/h)^2 - \sin^2\alpha\,]^{1/2}}{\cos\alpha} \qquad \text{(A14)}$$



Always consult and cite the final, published document. See http:/www.minsocam.org or GeoscienceWorld

and: $$\theta = \arcsin\left[\frac{\left[(a/h)^2 - \sin^2\alpha\,\right]^{1/2}}{\cos\alpha}\right] \tag{A15}$$

Differentiating (A15) with respect to $(a/h)$ gives:

$$\left|\frac{d\theta}{d(a/h)}\right| = \frac{(a/h)\,/\,\cos\alpha}{[1-(a/h)^2]^{1/2}\,[((a/h)^2 - \sin^2\alpha)/\cos^2\alpha]^{1/2}} \tag{A16}$$

Substituting (A14) and (A16) in (A13) gives:

$$N_T(a/h)\;d(a/h) = \frac{A\,(a/h)/\cos\alpha}{[1-(a/h)^2]^{1/2}}\;\;d(a/h) \tag{A17}$$

To obtain $N_T(h/a)\;d(h/a)$, we note that:

$$N_T(h/a)\;d(h/a) = N_T(a/h)\;\left|\frac{d(h/a)}{d(a/h)}\right|\;d(a/h) \tag{A18}$$

with: $$(h/a) = \frac{1}{(a/h)} \tag{A19}$$

and: $$\left|\frac{d(h/a)}{d(a/h)}\right| = \frac{1}{(h/a)^2} \tag{A20}$$

Substituting (A17), (A19) and (A20) in (A18) gives:

$$N_T(h/a)\;d(h/a) = \frac{A/\cos\alpha}{(h/a)^2\,[(h/a)^2 - 1]^{1/2}}\;\;d(h/a) \tag{A21}$$

<u>Appendix A4</u>. Exhumed tracks

For tracks exposed at the surface and etched due to surface etching (exhumed tracks), we have that (equation (7); main text):

$$N_E(\theta)\;d\theta = \;B\;d\theta \tag{A22}$$

And: $$N_E(\beta)\;d\beta = N_E(\theta)d\theta\;\left|\frac{d\theta}{d\beta}\right|\;d\beta \tag{A23}$$



Always consult and cite the final, published document. See http:/www.minsocam.org or GeoscienceWorld

$$N_E(g/b)\ d(g/b) = N_E(\theta) d\theta \ \left|\frac{d\theta}{d(g/b)}\right| \ d(g/b) \tag{A24}$$

$$N_E(a/h)\ d(a/h) = N_E(\theta) d\theta \ \left|\frac{d\theta}{d(a/h)}\right| \ d(a/h) \tag{A25}$$

Substituting (A5) and (A22) in (A23) gives:

$$N_E(\beta)\ d\beta = \frac{B\ \sin\alpha}{\sin^2\beta + \sin^2\alpha\ \cos^2\beta}\ d\beta \tag{A26}$$

Substituting (A11) and (A22) in (A24) gives:

$$N_E(g/b)\ d(g/b) = \frac{B\ (g/b)\ \tan\alpha}{[((g/b)^2 - 1) - \tan^2\alpha\ ]^{1/2}\ [(g/b)^2 - 1\ ]}\ d(g/b) \tag{A27}$$

Substituting (A16), (A20) and (A22) in (A25) gives:

$$N_E(a/h)\ d(a/h) = \frac{B\ /\ (h/a)\cos^2\alpha}{[(h/a)^2 - 1]^{1/2}\ [(1 - (h/a)^2\ \sin^2\alpha)]^{1/2}}\ d(a/h) \tag{A28}$$



Always consult and cite the final, published document. See http:/www.minsocam.org or GeoscienceWorld

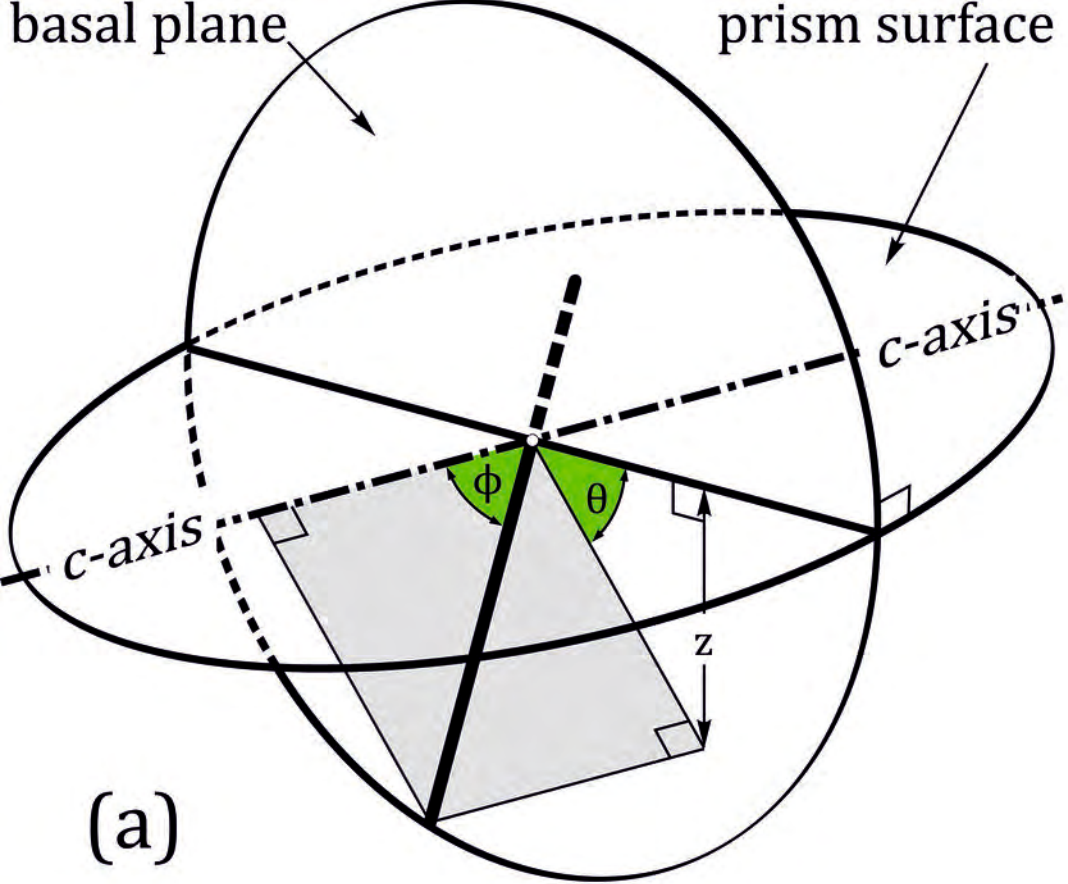

Figure 1

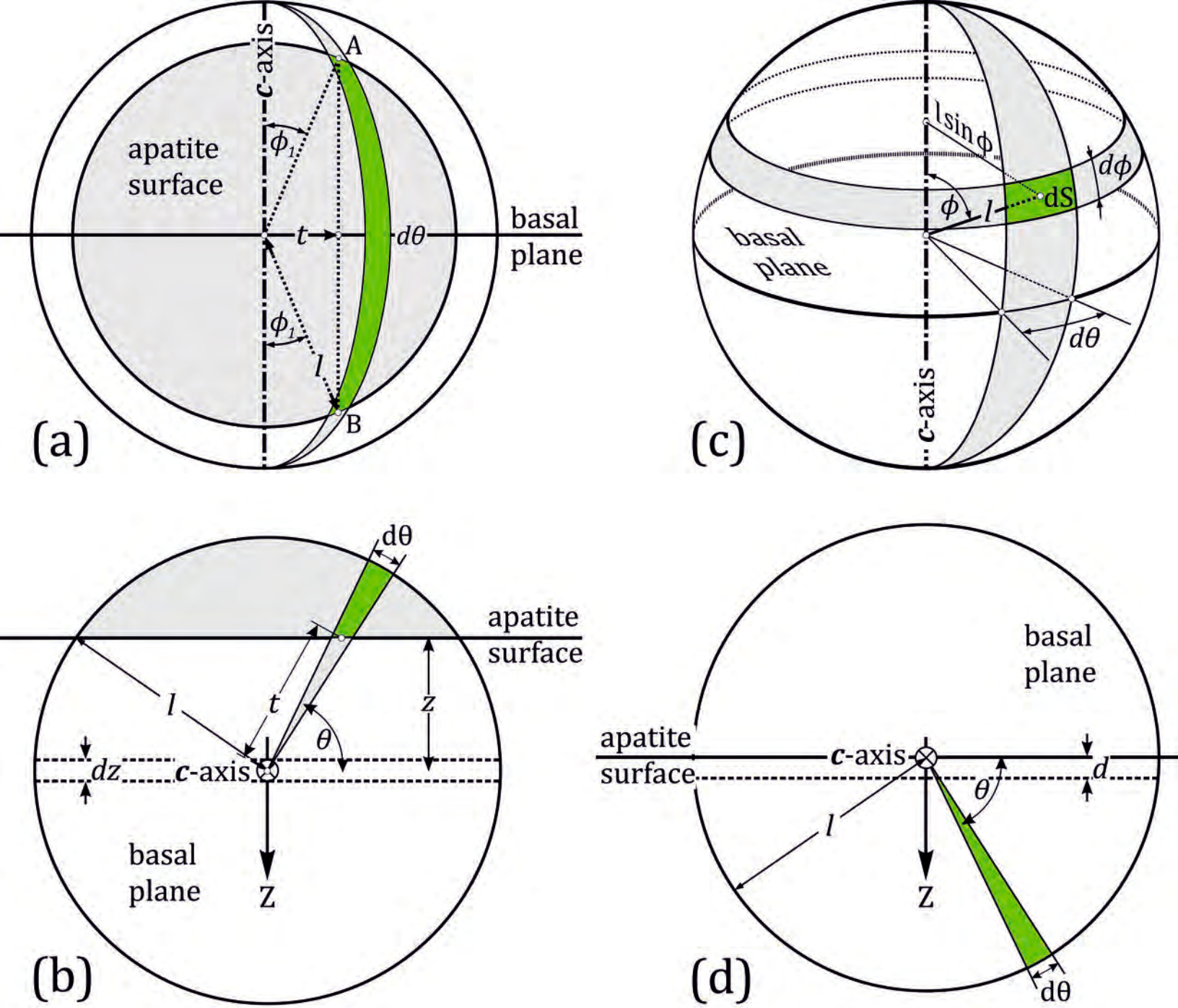
c-axis
A
apatite
surface
$\phi_1$
basal
plane
t
dθ
$\phi_1$
l
B
(a)
l sin ϕ
dϕ
ϕ
l
dS
basal
plane
dθ
c-axis
(c)
dθ
apatite
surface
l
t
z
θ
dz
c-axis
basal
plane
Z
(b)
basal
plane
apatite
surface
c-axis
d
θ
l
Z
dθ
(d)

Figure 2

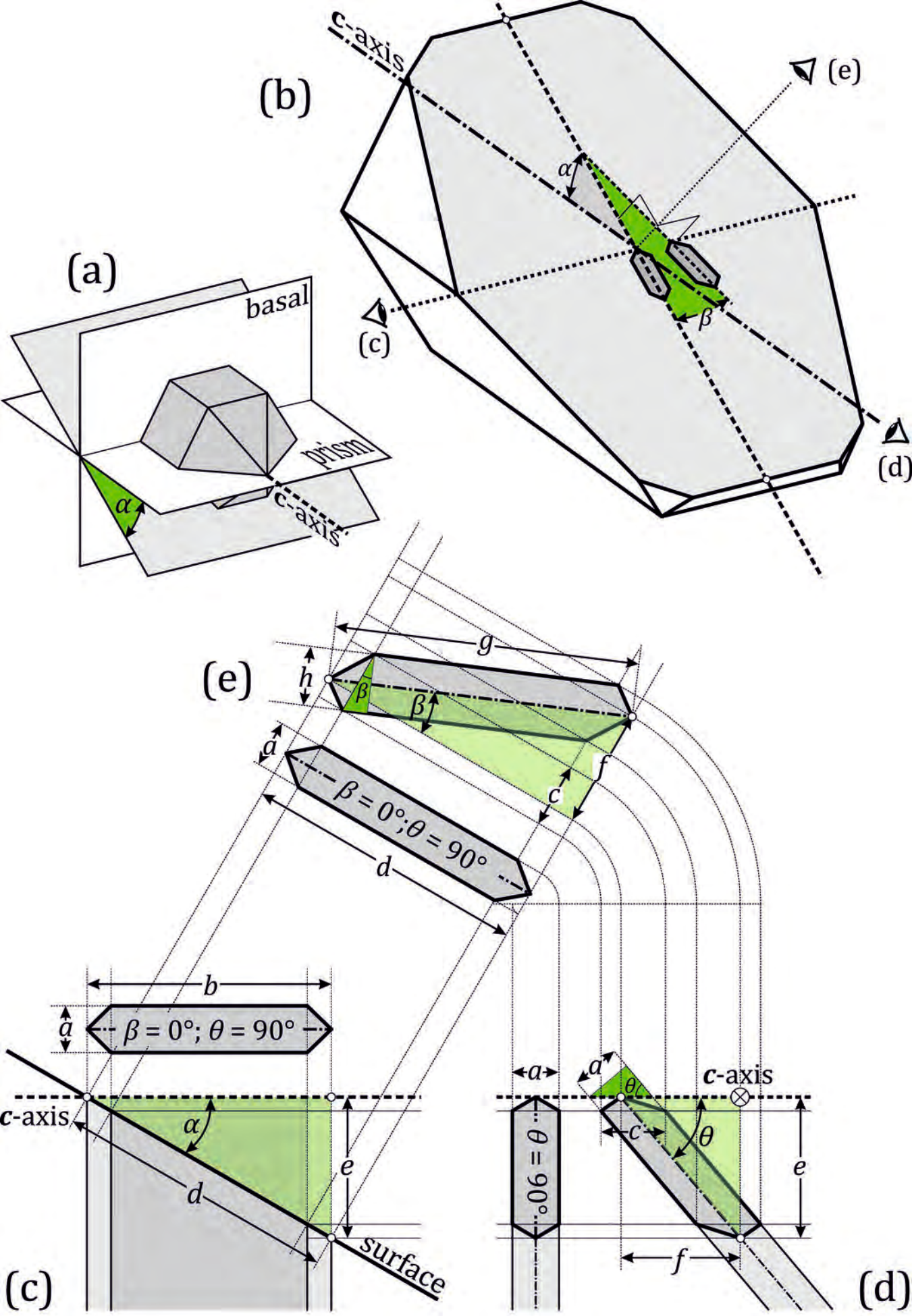
(a)
basal
prism
c-axis
α
(b)
c-axis
(e)
α
β
(c)
(d)
(e)
g
h
β
β
a
f
c
β = 0°; θ = 90°
d
b
a
β = 0°; θ = 90°
c-axis
α
d
e
surface
(c)
a
a
θ
c-axis
c
θ
θ = 90°
e
f
(d)

Figure 3

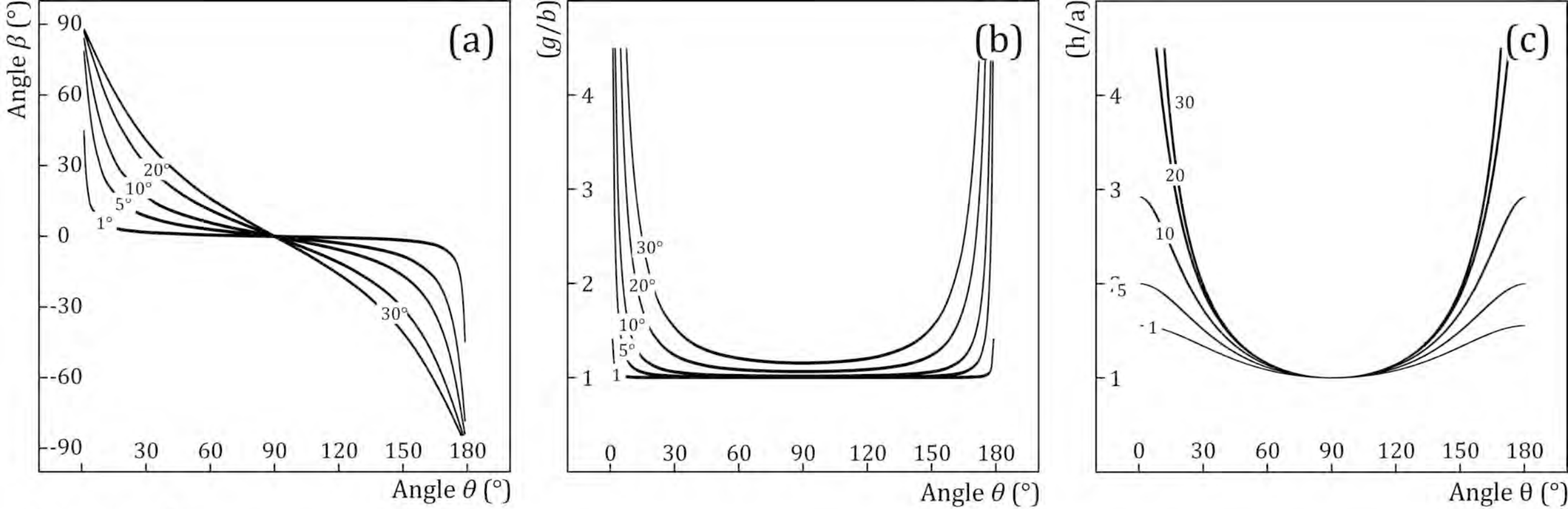
(a)
Angle β (°)
90
60
30
0
-30
-60
-90
20°
10°
5°
1°
30°
30
60
90
120
150
180
Angle θ (°)
(b)
(g/b)
4
3
2
1
30°
20°
10°
5°
1
0
30
60
90
120
150
180
Angle θ (°)
(c)
(h/a)
4
3
1
30
20
10
5
1
0
30
60
90
120
150
180
Angle θ (°)

Figure 4

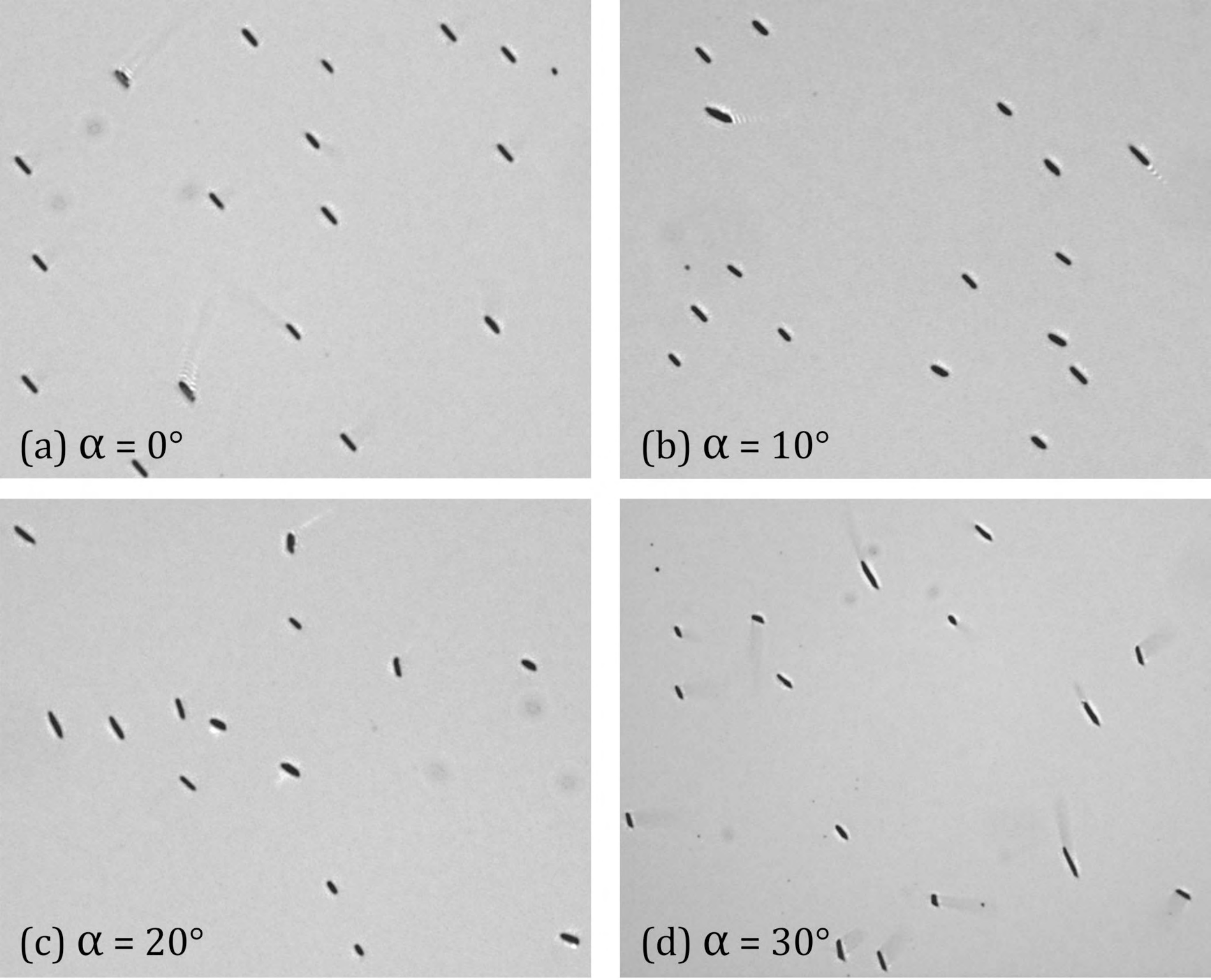


Figure 5

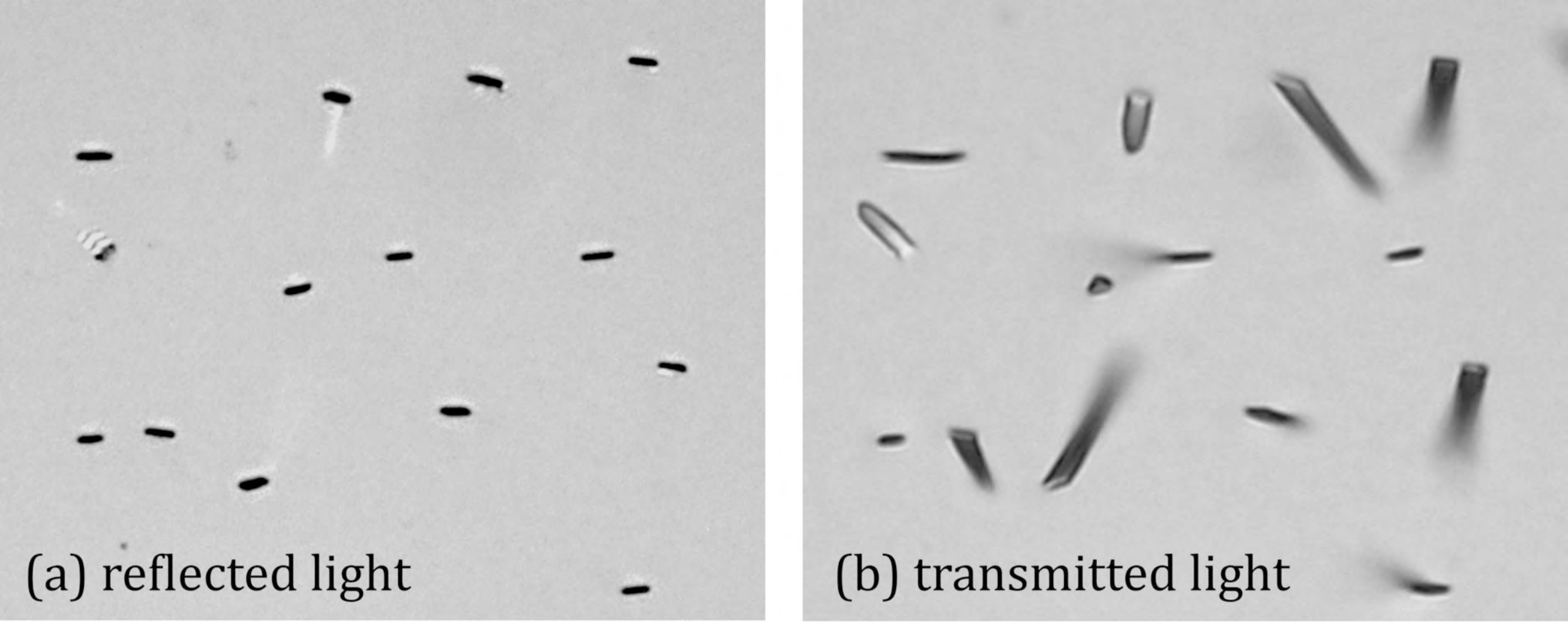


Figure 6

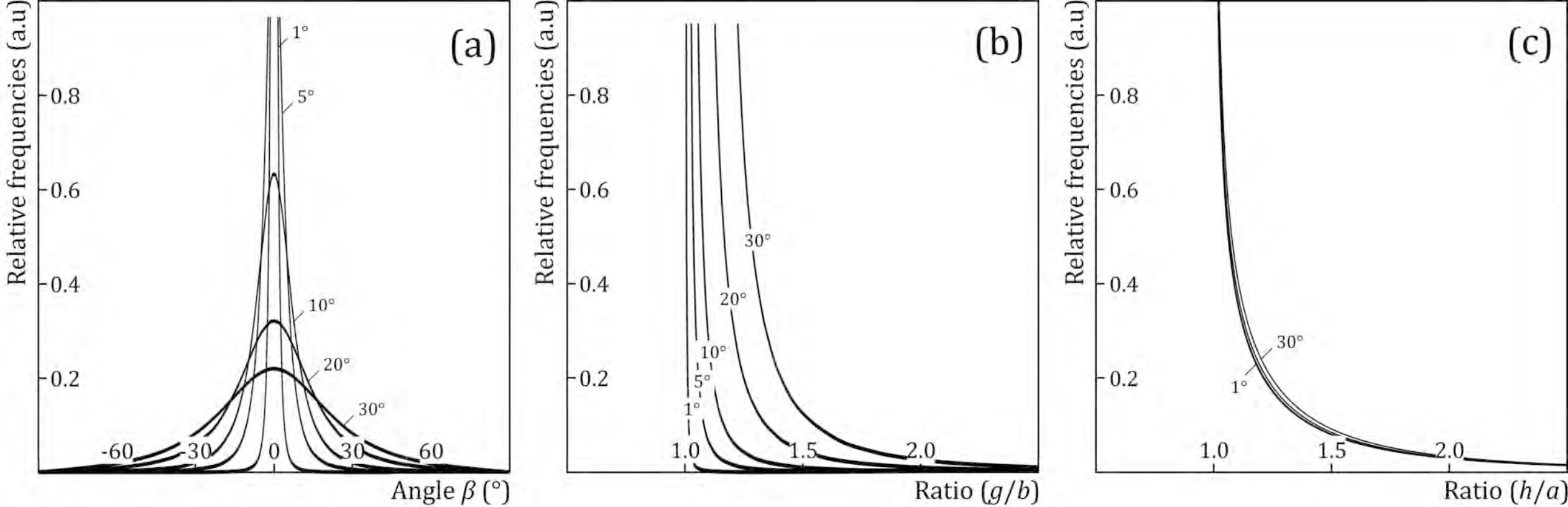
(a)
Relative frequencies (a.u)
0.8
0.6
0.4
0.2
1°
5°
10°
20°
30°
-60
-30
0
30
60
Angle β (°)
(b)
Relative frequencies (a.u)
0.8
0.6
0.4
0.2
30°
20°
10°
5°
1°
1.0
1.5
2.0
Ratio (g/b)
(c)
Relative frequencies (a.u)
0.8
0.6
0.4
0.2
30°
1°
1.0
1.5
2.0
Ratio (h/a)

Figure 7

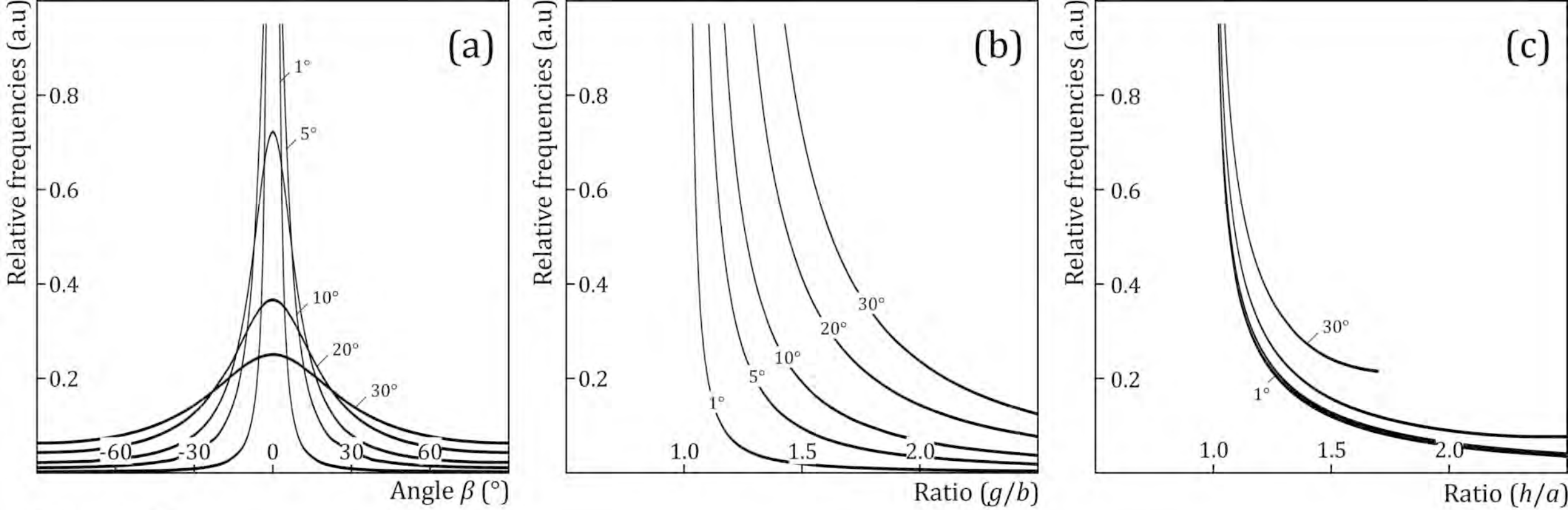
(a)
Relative frequencies (a.u)
0.8
0.6
0.4
0.2
1°
5°
10°
20°
30°
-60
-30
0
30
60
Angle β (°)
(b)
Relative frequencies (a.u)
0.8
0.6
0.4
0.2
1°
5°
10°
20°
30°
1.0
1.5
2.0
Ratio (g/b)
(c)
Relative frequencies (a.u)
0.8
0.6
0.4
0.2
30°
1°
1.0
1.5
2.0
Ratio (h/a)

Figure 8

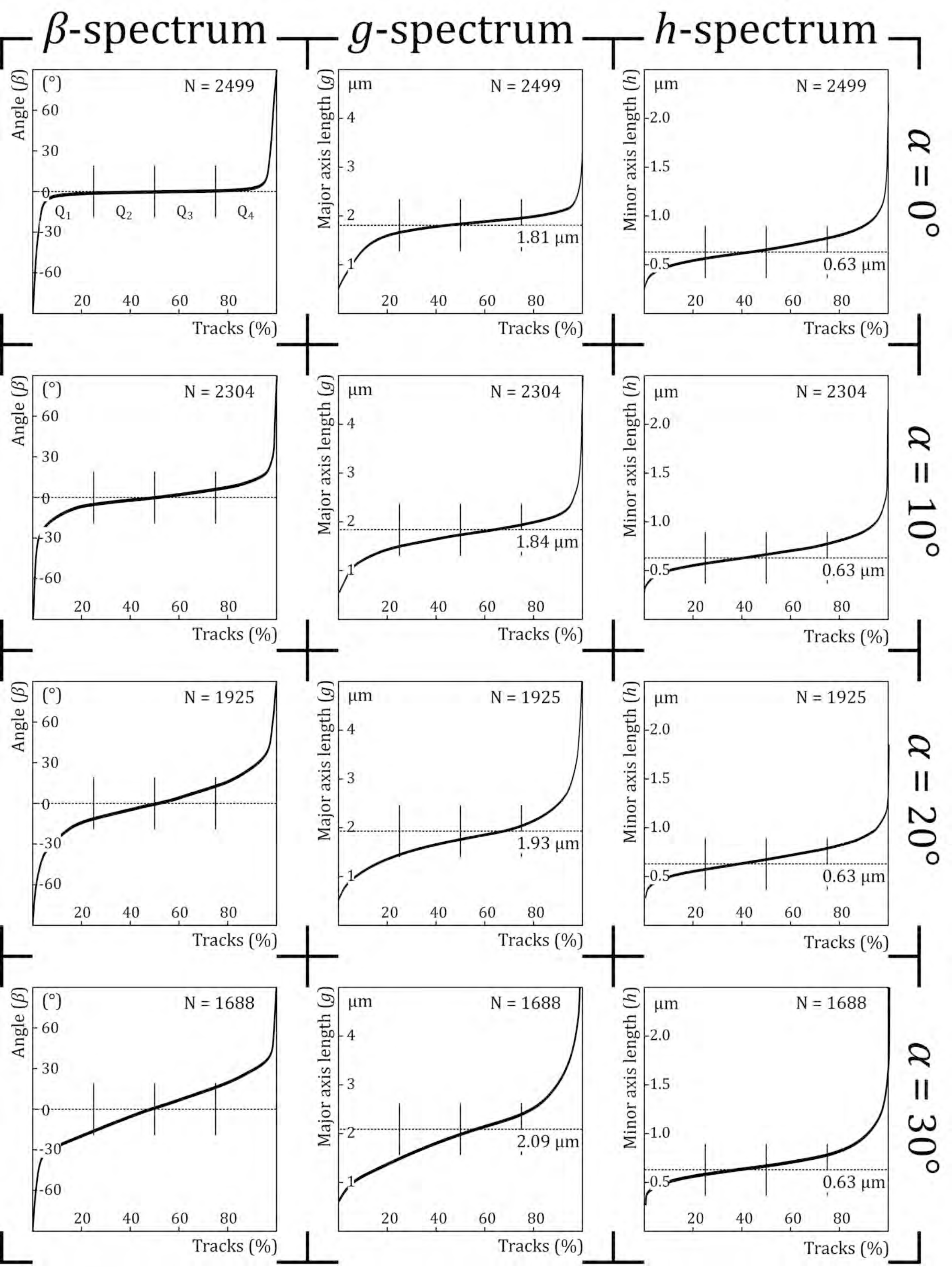
β-spectrum
g-spectrum
h-spectrum
α = 0°
α = 10°
α = 20°
α = 30°
Angle (β)
Major axis length (g)
Minor axis length (h)
(°)
µm
N = 2499
N = 2304
N = 1925
N = 1688
Q1
Q2
Q3
Q4
1.81 µm
1.84 µm
1.93 µm
2.09 µm
0.63 µm
Tracks (%)

Figure 10

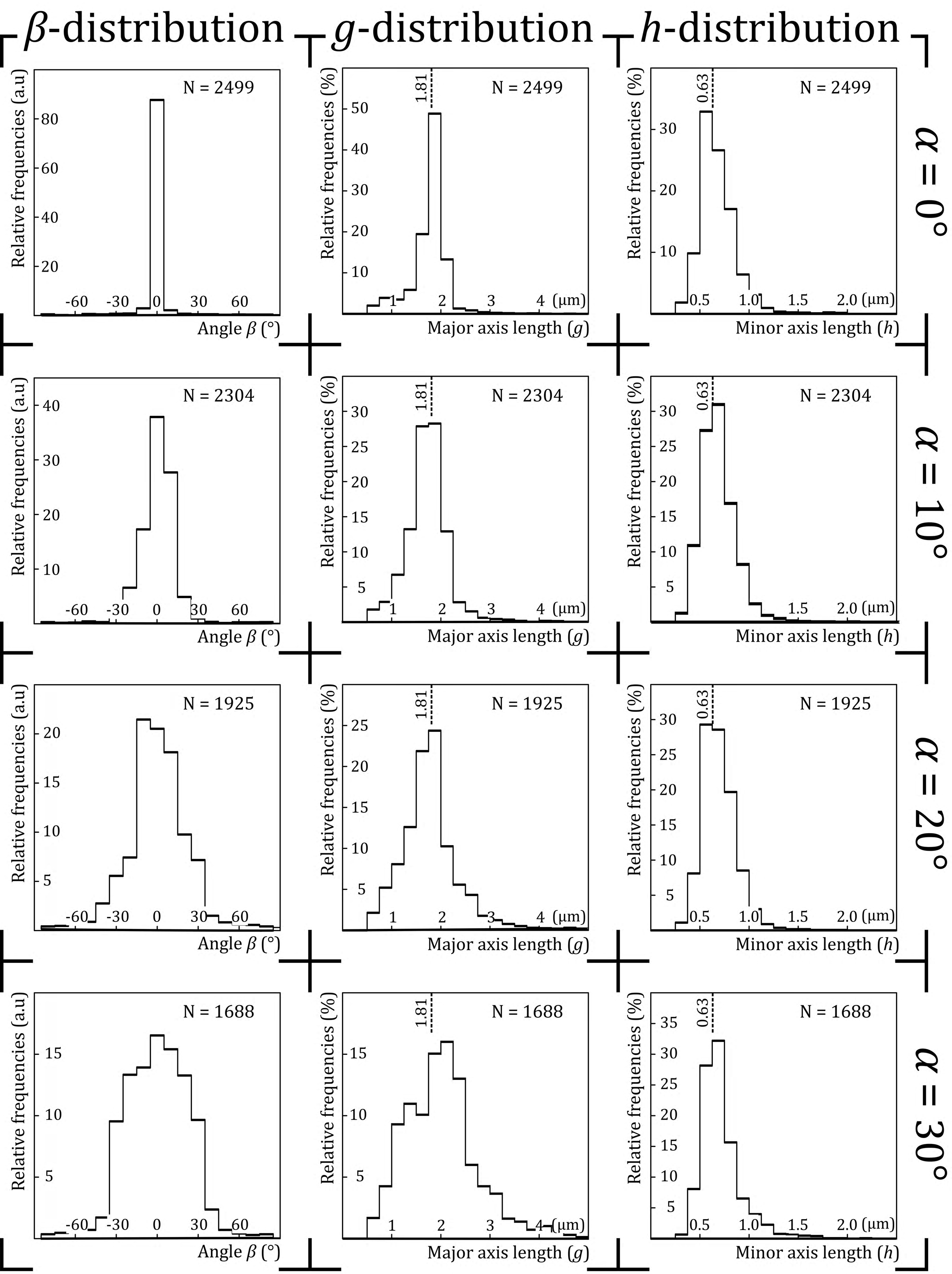
β-distribution
g-distribution
h-distribution
α = 0°
α = 10°
α = 20°
α = 30°
N = 2499
N = 2304
N = 1925
N = 1688
1.81
0.63
Relative frequencies (a.u)
Relative frequencies (%)
Angle β (°)
Major axis length (g)
Minor axis length (h)
(μm)

Figure 9